Optimizing Wavelengths for Optics-based Measurements of Advanced Electronics

Bryan M. Barnes

Nanoscale Device Characterization Division, National Institute of Standards and Technology, 100 Bureau Drive MS 8423, Gaithersburg, MD 20899-8423, USA

ABSTRACT

The semiconductor industry has just recently met the end of "Moore's Law", the cyclical reduction in transistor cost observed over several decades. New architectures, materials combinations, and limited dimensional scaling are anticipated over the next decade to realize smaller, energy-efficient, high-performance, and secure devices. These changes extend not only to the advanced gate stack but also to the metal interconnects in the back-end-of-line, or BEOL. Two simulation studies using wavelengths from the ultraviolet to the infrared yield the anticipated optical response from two metal line width extremes presented in recent literature. First, simulated images of micrometer-scale Cu interconnects are compared qualitatively with a published experimental image to illustrate challenges in applying shorter visible and ultraviolet wavelengths. Second, tailoring the linear polarization axes and incident angles enables comparable or better sensitivities to line width changes using ultraviolet light relative to infrared illumination for nanoscale periodic Ru and Cu lines with air gaps. The optical response of Cu lines buried about 1 μm in SiO_2 are compared, indicating that optical density might be integral to utilizing deep ultraviolet wavelengths for characterizing such interconnects.

Keywords: Optical scattering, metal interconnects, electromagnetic simulation, scatterfield microscopy, normalized sensitivity

1. INTRODUCTION

Fabricating modern semiconductor chips starts with a bare silicon surface, proceeds through multiple photolithographic steps, and ends at packaging requiring numerous metrology techniques[1] and steps. Within this workflow, diverse metrology challenges exist given the various lengths scales and multiple materials involved, not only in the plane of the semiconductor wafer (defined using coordinates (x, y)) but also perpendicular to this plane (z). When constructing transistors with near atomic-scale dimensions, key measurements include the detection of patterning errors that already render chips unusable (known as defect inspection), the determination of $(\Delta x, \Delta y)$ dimensional offsets between subsequent lithographic patterning layers (overlay metrology), and the accurate measurement of line widths at the sub-15 nm scale (critical dimension metrology). An industrial term for this region in which the advanced gate stack is fabricated is the "front-end-of-line" or FEOL, alluding to its order in this workflow. For the FEOL, optical methods have proven ideal for fast, non-destructive, and inexpensive measurements over the relatively large areas of the wafer compared to the sizes of these nanoelectronic devices.

However, these highly sophisticated semiconductor architectures at the FEOL are useless without interconnections among them and with the outside world. There are multiple layers of metallic interconnects required to facilitate the flow of electric current to, from, and among these FEOL devices, and this region is termed the "back-end-of-line" or BEOL. Linewidths for these interconnects vary greatly within the BEOL. The last fabricated layers of metal interconnects must have length scales tailored for efficient electrical contact with the chip's packaging, while the periodic spacing of the first layers matching FEOL device dimensions, with 32 nm metal pitch interconnects anticipated for production by 2027.[1] The region of interconnects closest to the FEOL may also be considered as the "middle-of-line" or MOL, a subset of the BEOL. Colleagues at the National Institute of Standards and Technology (NIST) address specific metrology challenges of the BEOL through electrical test and scanned probe measurements, including examinations of Cu electromigration[2] and scanned probe imaging of buried interconnects.[3]

E-mail: bmbarnes@nist.gov, Telephone: 1 301 975 3947

In this paper, electromagnetic simulation studies are performed to assess the extensibility of our optics-based approaches to cutting-edge research at the MOL and BEOL. Two imaging studies address the dimensional extremes and specific challenges of utilizing optical scattering for interconnects, with each study based on a recent report in the literature. Wavelengths ranging from the ultraviolet to the infrared are simulated to determine optimal wavelength ranges, noting that for our FEOL research custom-build microscopes have been developed in-house with λ = 193 nm[4] and λ = 450 nm. Prior to experimentally realizing a customized tool for the BEOL, additional simulation studies would be required to incorporate available wavelength-dependent optical configurations into our analysis. This work instead utilizes a "best-case" approach to discern how applicable specific wavelengths or wavelength ranges are to anticipated MOL and BEOL research over the next decade, especially as the current interconnect metal, Cu, is potentially replaced.

2. INTERCONNECT EXAMPLES AND THEIR SIMULATION GEOMETRIES

2.1 Back-end-of-line (BEOL) Example

NIST colleagues have imaged buried interconnects capacitively with scanned microwave microscopy (SMM) as illustrated in Fig. 1, further augmented with electrostatic force (EFM)/ Kelvin force microscopy. SMM is passive with no applied voltages, while EFM requires an applied electric field. Combined, these techniques have potential to detect unintentional buried opens or shorts for failure analysis. Both are scanned probe microscopy techniques applied in that work to a "staircase" of Cu interconnects, some of which were buried in SiO_2 as shown in Fig. 1(a,b). Figure 1(d) shows the successful imaging of Cu lines buried 0.97 μm and 1.84 μm below the surface of this test structure.

Their optical microscope image, Fig. 1(e), which is assumed to be under white-light illumination clearly images these buried lines as well. Specifically, exposed Cu lines (region M3) appear bright with a green tint; it can be shown that bare Cu reflects at all wavelengths studied here but is most intense for wavelengths longer than 575 nm. Buried Cu lines appear either dark green (M2) or red (M1), potentially indicating constructive interference in addition to the preferential reflection of longer wavelengths. Likewise, the SiO_2-covered Si can also be shown to reflect visible wavelengths with more intensity at shorter (e.g., blue) wavelengths as seen here.

Two-dimensional simulation geometries are illustrated to scale as Fig. 1(c). Eight distinct slices were selected to examine the imaging of an isolated Cu micrometer-scale line in the presence of a Cu cross-line (Slice A), with direct Cu-to-air contact (Slices A-E), at junctions (Slices D, E, and G), under almost 1 μm of SiO_2 (slices F and G), and under almost 2 μm of SiO_2 (slice H).

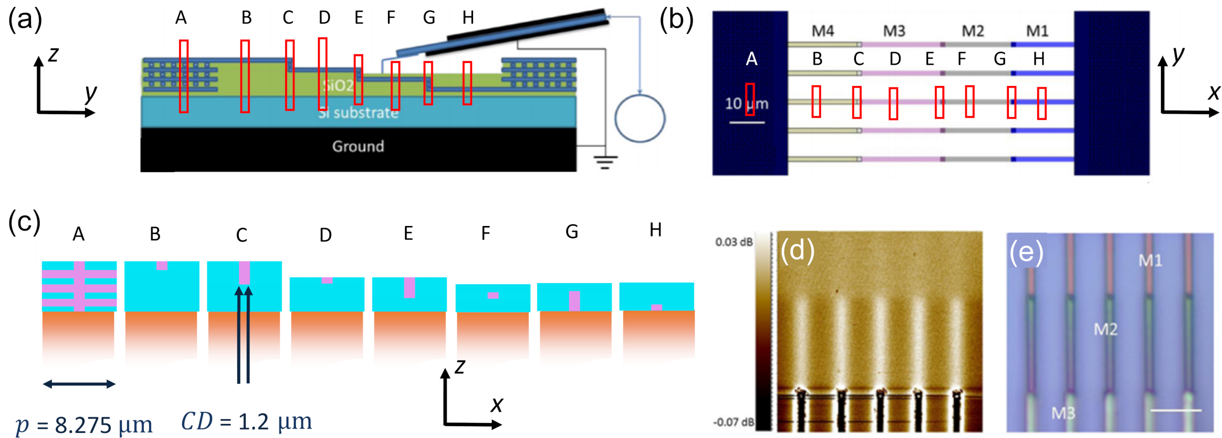

Figure 1. Schematics, experimental measurements, and optical simulation strategies for a BEOL research sample. (a) Schematic side view of Cu lines in SiO_2 showing buried layers measured using a scanning probe. Eight 2-D slices are identified with rectangles labeled A-H for simulation. (b) Schematic top-down view. (c) Optical simulation geometries shown to scale, orthogonal to the plane in Panel (a). (d) Scanned microwave microscopy of buried features up to 2 μm in depth (e) Optical experimental image which also shows these buried features. All panels except (c) reprinted from Ref. 3

2.2 Middle-of-line (MOL) Example

In early 2021, Leśniewska, *et al.* have published[5] an experimental report on the reliability of direct metal-etched Ru semidamascene interconnects in preparation for the upcoming 2-nm semiconductor fabrication node. Cross-sectional information from that paper has been summarized using the schematic in Fig. 2(a). These Ru lines are insulated from one another by air gaps nominally 16 nm in width. This configuration reduces the interconnect resistivity relative to contemporary dual damascene Cu lines, reducing wasted energy through Joule heating. The reported thickness of the upper layers are 5 nm for SiCN, 20 nm for SiCO, 50 nm for the first SiN layer, 300 nm of SiO_2, then 500 nm for a second SiN layer. The dimensions as shown comport with the transmission electron microscope image in Ref. 5 for which its overlayer is approximately 25 nm, possibly suggesting that the SiCN/SiCO overlayer might be sufficient for forming the air gap; in addition, an underlayer of organosilicate glass (OSG 3.0) is included that was shown in their TEM image.

Figures 2(b-f) are variations on their nominal structure summarized in Fig. 2(a). To facilitate understanding, the complicated overlayer and the OSG 3.0 underlayer have been assumed to be SiO_2, concentrating our attention on the air gap and the Ru lines capped with TiN and a SiN line. The layer below the OSG 3.0 was not identified and thus Si was chosen for this study following our BEOL study. It is important to ascertain whether the wavelengths to be utilized can measure such Ru structures as they are the likely future of the MOL/BEOL, but a second set of simulation within this study replaces Ru with Cu to identify wavelengths suitable for either material. The role of the air gap is explored through a third series of simulations, while a baseline is established by simulating a solid SiO_2 layer atop Si.

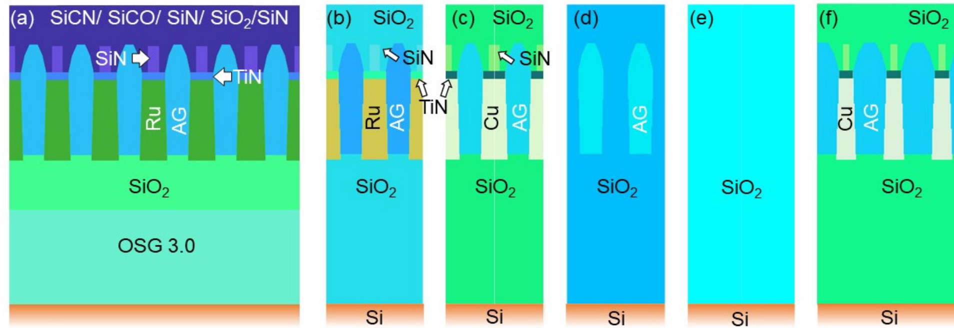

Figure 2. Schematic layout for MOL Ru interconnects buffered with air gaps (AG) defined from a transmission electron microscopy (TEM) image in Ref. 5, with various optical simulation strategies. (a) Materials and geometric specifications for the published Ru interconnects with an underlayer of organosilicate glass (OSG 3.0) on an unspecified substrate. (b) A simplified version of the nominal structure for simulation augmented using (c) replacement of Ru with Cu and (d) reductions to SiO_2 and the AG as well as (e) a "Null" case. (f) Simulation geometry after AG widths are increased 30 % as defined in Table 1; SiN widths are scaled proportionally.

Table 1. Dimensions in the MOL interconnects, air gaps (AG), and other features from Fig. 2. In the simulation study, the air gap widths (AG) have been scaled between between 1.0 and 1.3. The critical dimension (*CD*) here is $w_{\mathrm{Ru}_{\mathrm{mid}}}$.

Scaling Factor	Widths (nm)							Heights (nm)			
	$w_{\mathrm{AG}_{\mathrm{top}}}$	$w_{\mathrm{AG}_{\mathrm{max}}}$	$w_{\mathrm{AG}_{\mathrm{bot}}}$	w_{SiN}	$w_{\mathrm{Ru}_{\mathrm{top}}}$ [a]	$w_{\mathrm{Ru}_{\mathrm{bot}}}$	$w_{\mathrm{Ru}_{\mathrm{mid}}}$	h_{AG}	h_{SiN}	h_{TiN}	h_{Ru}
1.0	5.4	16.7	13.5	7.6	14.7	18.1	16.4	71.5	16.9	5.0	57.2
1.1	5.9	18.3	14.9	6.8	13.0	16.8	14.8	unchanged			
1.2	6.5	20.0	16.2	5.9	11.3	15.4	13.3	unchanged			
1.3	7.0	21.7	17.6	5.1	9.6	14.1	11.8	unchanged			

[a] same as w_{TiN}

There are two key sets of dimensional changes in this MOL simulation study. First, the thickness of the overlayer is varied to emulate imaging at different points during fabrication. Four thicknesses, t, of overlayer are presumed fron Ref. 5: 25 nm (for SiCN/SiCO), 75 nm (adding SiN), 375 nm (adding SiO_2), and 875 nm (including all layers). Second, we perform four distinct scalings of the width of the air gap, increasing the width of its base ($w_{\mathrm{AG_{bot}}}$) by a factor of 1.0 to 1.3 in steps of 0.1; with constant pitch, scaling increases reduce the widths of the Ru (or Cu or SiO_2) lines. The resultant dimensions for the air gap, Ru, TiN, and SiN are provided as Table 1. These geometrical variations lead to a total of 13 distinct simulation geometries, as AG scaling has no effect on the "Null" case of SiO_2 on Si.

3. SIMULATION STUDY METHODOLOGIES

There are common elements and distinctive differences between the simulation studies performed using these BEOL and MOL examples. Commonalities include the assumption of a high-magnification imaging platform and a commonly defined coordinate system as illustrated in Fig. 3(a) and 3(b), respectively. Both studies are performed using an implementation[6] of rigorous coupled-wave analysis[7,8] (RCWA) in two dimensions, assuming infinitely long periodic lines. The incident light is linearly polarized either along the line (x axis) or across the line (y axis). Optical constants are from the literature and shown as Figs. 3(c) and 3(d), with constants for Cu, SiO_2, and Si shared between the simulation sets.

Differences between the studies include the angle(s) of incidence as well as the illumination and collection numerical apertures (INA, CNA). For the BEOL, to better emulate the experimental image in Fig. 1(e), the INA and CNA were set to 0.95. For the MOL, angular scanning within a high magnification platform is assumed. Experimentally, this is achieved by establishing Köhler illumination and scanning an aperture (not shown) at a conjugate to the objective's back focal plane defining both the incident angle at the sample and the off-axis INA. This is one realization[9] of scatterfield microscopy[10] (SM), in which the three-dimensional scattered field from sub-wavelength features is optimized for metrology. SM can include the tailoring of the incident polarization and incident angles as well as selection of focus position(s). SM also couples these enhancements with customized target design, materials choices, and geometrical foreknowledge. For the MOL simulations the INA = 0.13, following prior experimental work[9] we have reported at $\lambda = 450$ nm. CNA was set to unity. Angles of incidence are defined either along the axis (i.e., θ_x, scanning perpendicular to the line) or along the y axis (θ_y, scanning parallel to the line). An "X scan" is a set of measurements along θ_x with $\theta_x = 0°$, with a "Y scan" along θ_y with $\theta_x = 0°$. For BEOL, $\theta_x = \theta_y = 0°$.

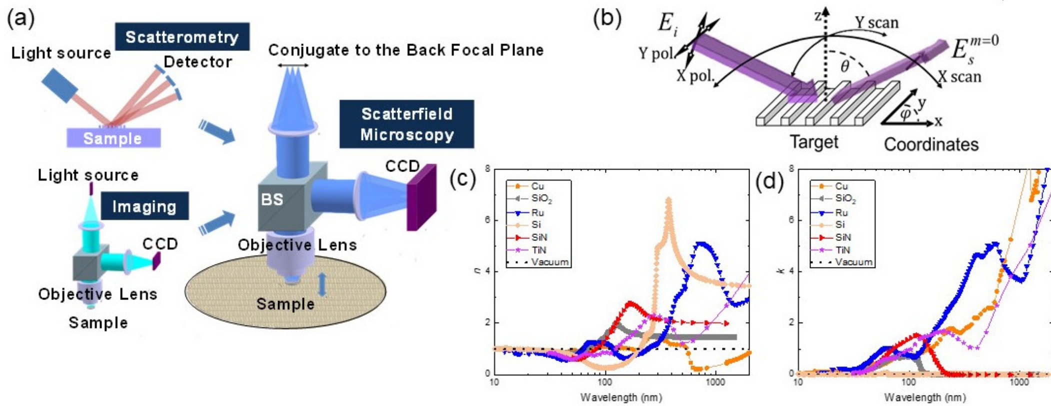

Figure 3. Optical systems, coordinates, and constants utilized in the simulations. (a) Schematic of scatterfield microscopy realized in angle-scanning mode. A high-magnification platform with beamsplitter (BS) and charge-coupled device (CCD) sensors achieves angular resolution by scanning an aperture at the conjugate to the objective's back focal plane with Köhler illumination, effectively yielding scatterometric capabilities. From Ref. 11. (b) Coordinates defined from sample orientation. While scatterometry collects the 0th order scattering shown (purple arrows), scatterfield microscopy can collect higher orders also. From Ref. 12. (c,d) Optical constants (n, k) from Refs. 13 (Cu), 14 (SiO_2), 15 (Ru), 16 (Si), 17 (SiN), 18 (TiN). Fitted lines are shown to guide the eye.

Other major differences include the simulation domain size, the simulated focal positions, the addition of noise intensity, and the number of wavelengths investigated. The simulations differ in their dimensions, with the BEOL geometry featuring a relatively large period $p = 8.275$ μm for simulating these isolated lines, while the MOL geometry features a dense, periodic grating with $p = 31.6$ nm. For both the BEOL and MOL, images have been simulated with the focus position at the top of the simulation domain for simplicity, but an additional image is calculated for the top of the buried Cu line in the BEOL study for comparison. No noise has been applied to the BEOL, while Gaussian noise ($\mu = 3 \times 10^{-2}$ $I_0, \sigma = 7 \times 10^{-3}$ I_0) was added to the MOL results for quantitative analysis. Both studies utilized 200 nm and 450 nm wavelengths as these are close to or match current experimental wavelengths. For the BEOL study, $\lambda =$ 135 nm, 300 nm, and 1000 nm are added to these values. These five wavelengths are sufficient for a qualitative comparison against experimental data from Ref. 3. For the MOL study, 14 additional wavelengths ranging from $\lambda = 35$ nm to $\lambda = 2000$ nm are added for nineteen total wavelengths.

The scaling of the air gap and the variation in SiO_2 overlayer thickness, t, in the MOL study facilitates quantitative analysis. The initial figure of merit is the sensitivity S defined here as

$$S(\lambda, \alpha, \phi, t) = \frac{\Delta I(\lambda, \alpha, \phi, t)}{\bar{I}(\lambda, \alpha, \phi, t)} = 2\frac{I_1(\lambda, \alpha, \phi, t) - I_2(\lambda, \alpha, \phi, t)}{I_1(\lambda, \alpha, \phi, t) + I_2(\lambda, \alpha, \phi, t)}, \tag{1}$$

where intensities I_1 and I_2 are from two separate measurands under test at a given wavelength λ, incident angle α, and linear polarization pass axis ϕ. For this quantitative analysis, the $w_{Ru_{mid}}$ will be the critical dimension (CD) and applied more generally across the Ru, Cu, and air gap geometries. With a CD defined for each measurand, the sensitivity can be normalized to the CD, yielding a related but second metric. The normalized sensitivity NS is

$$NS(\lambda, \alpha, \phi, t) = S(\lambda, \alpha, \phi, t)\frac{\Delta CD}{\overline{CD}} = 2S(\lambda, \alpha, \phi, t)\frac{CD_1 - CD_2}{CD_1 + CD_2}, \tag{2}$$

where two critical dimensions CD_1 and CD_2 scale the sensitivity S, allowing better comparison among measurands with different ΔCD.

4. SIMULATION STUDY RESULTS

4.1 BEOL Example

Figure 4(a) shows an array of one-dimensional images corresponding to simulations at a particular wavelength and slice location (cf. Fig. 1). For Slices A-E, each wavelength images the exposed Cu line; Slices B,C are not shown in Fig. 4(a) as they closely match Slices D,E. For $\lambda \geq 200$ nm, the Cu cross-line affects the image in Slice A, indicating that $\lambda = 135$ nm is insensitive to the buried cross-line. The simulations also show $\lambda = 135$ nm cannot image the buried line in Slices F-H. Comparing Slice F to Slice E, the simulated intensity from these isolated CD = 1.2 μm lines is reduced for $\lambda \leq 300$ nm, illustrating challenges to imaging such buried lines with UV wavelengths. The image at $\lambda \leq 450$ nm has less intensity at Slices F-H even when attempting better focus. Properly focused, only $\lambda = 1000$ nm can image Slices F-H.

Qualitatively, the results in Fig. 4(a) for Slices D-H are consistent with the experimental image in Figure 4(b) from Ref. 3. Arrows guide the eye to the corresponding locations for the Slices relative to the experimental image. As discussed in Section 2.1, the experimental image at Slices D and E have a green-tinted but broad-spectrum optical response as expected, and the line is imaged in simulation at all wavelengths for these slices. Comparison with Slices F-H is less straightforward due to the SiO_2, which ideally from Fig. 3(d) should have negligible attenuation ($k < 0.01$ for $\lambda > 180$ nm). At Slices F and G however, the experimental image of the line is a darker green which does compare favorably with the reduced intensities realized at ultraviolet and visible wavelengths. The less-intense imaging of the line in simulation at Slice H at $\lambda \leq 450$ nm is also consistent with, but not explained by, the experimental image. While a full assessment of the experimental image lies beyond the scope of this work, both simulation and experiment suggest that these relatively isolated buried Cu interconnects may be better accessed using longer wavelengths.

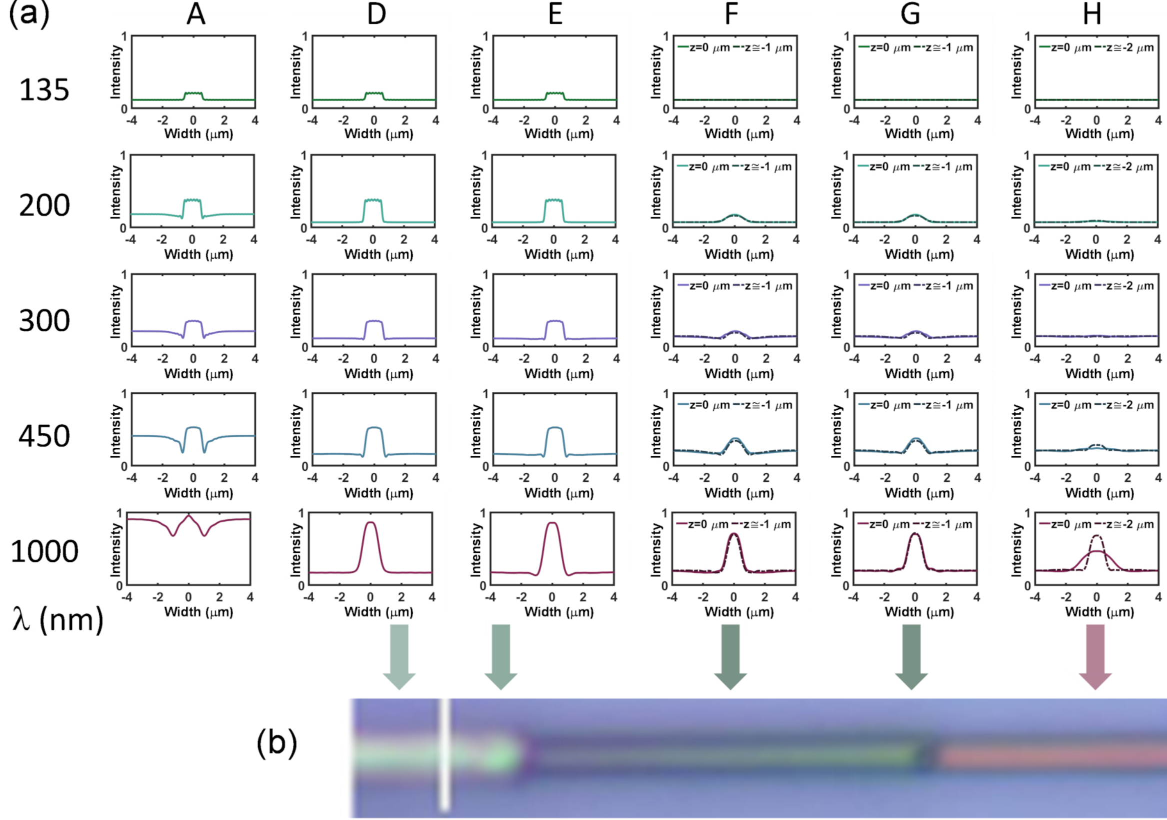

Figure 4. (a) Simulated image cross-sections for six of the eight BEOL simulation slices, as cases B-E are essentially equivalent. (b) Inset of the optical experimental image in Fig 1(e) from Ref. 3 with arrows corresponding to regions simulated. Both simulation and experiment indicate reduced intensities for short wavelengths ($\lambda \leq 450$ nm) consistent with the known strong optical response from bare Cu for $\lambda \geq 575$ nm.

4.2 MOL Example

In light of the BEOL result, the results for an SiO_2 thickness of $t = 25$ nm above the air gap are examined first is to determine the utility to the ultraviolet or short visible wavelengths in imaging MOL features. Figure 5 shows angle scans in θ_x for the air gap (AG), Ru, and Null cases for the two simulation wavelengths closest to our experimental wavelengths of $\lambda = 193$ nm and $\lambda = 450$ nm. The optical response of the Ru and the air gap are less correlated in Fig. 5(a) for $\lambda = 200$ nm than in Fig. 5(b) for $\lambda = 450$ nm, a possible indication that the metal at $\lambda = 450$ nm does not contribute as strongly to the intensity. In Fig. 5(d), the optical response does not change greatly at $\lambda = 450$ nm even with $\Delta CD = 4.6$ nm. With an optimized linear polarization direction (pol_y) and scan axis (X scan), the change in the intensity at $\lambda = 200$ nm is much more promising.

The sensitivity between the curves in Fig. 5 can be compared point-by-point using Eq. 1, *i.e.*, for each polarization, incident angle, and SiO_2 thickness t. To quantitatively assess these observed trends over the full range of 19 simulated wavelengths, these sensitivity data will be consolidated to a scalar value

$$S(\lambda, t) = \sum_{i}^{N} \sum_{j}^{P} \frac{S(\lambda, \alpha_i, \phi_j, t)}{NP}, \tag{3}$$

where N is the number of angles considered and P is the number of polarization axes considered. In this work, the sensitivity metric will only be calculated for measurands with the same t, thus $S(\lambda)$. As one linear polarization direction (y-pol) proved useful for $\lambda = 200$ nm, data from that polarization will be used exclusively in Fig. 6 while summing over the $N = 20$ angles in the y-scan to determine an average $S(\lambda)$.

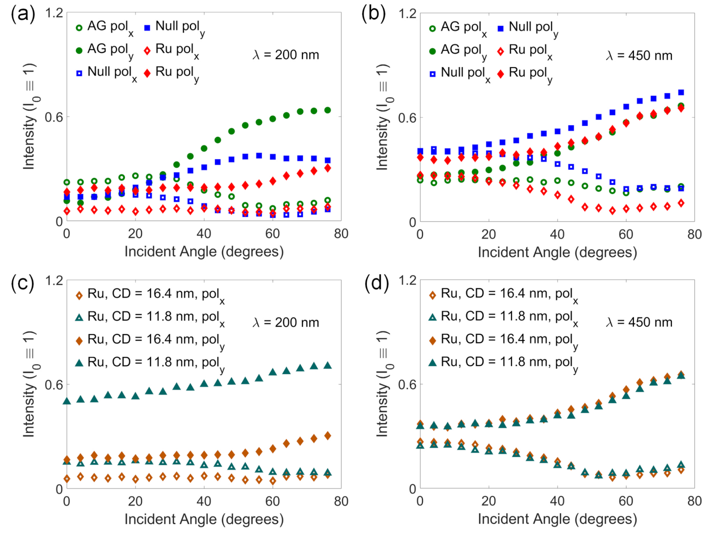

Figure 5. Intensity as a function of incident angle at CD = 16.4 nm and air gap (AG), "Null", and Ru geometries for wavelengths (a) 200 nm and (b) 450 nm. The AG and Ru results are similar at $\lambda = 450$ nm but different for $\lambda = 200$ nm. Here, the optimal angle scan axis is shown (θ_x). Comparison of CD = 16.4 nm vs CD = 11.8 nm for Ru lines using wavelengths (c) 200 nm showing a large response for light polarized parallel to the line (i.e., $\mathrm{pol_y}$) which is not seen at (d) 450 nm.

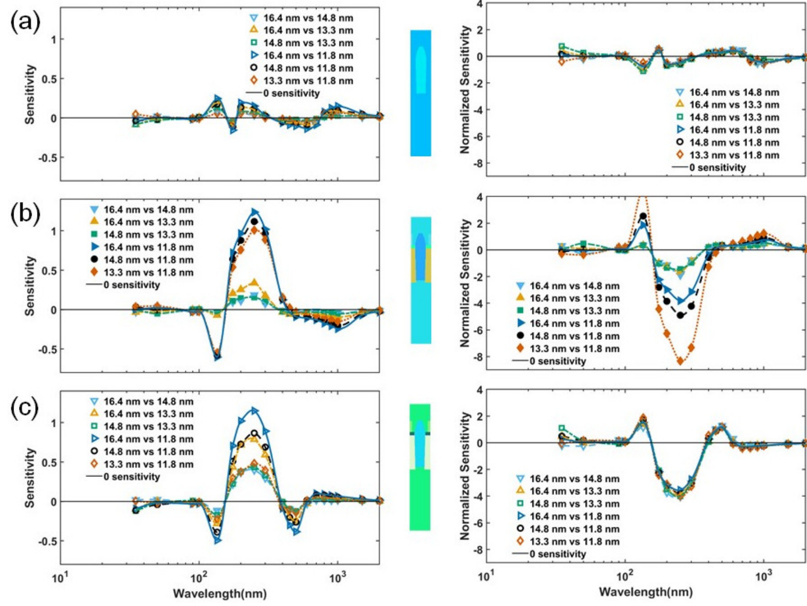

Figure 6. Sensitivity and Normalized Sensitivity as functions of wavelength for fixed angle scan axis ($\alpha = \theta_{x,1}, \ldots, \theta_{x,N}$) (cf. Eq. 3) and linear polarization axis ($\phi = \mathrm{pol_y}$) for the four scaling factors and resulting six possible comparisons. Rows again correspond to (a) Air gap (AG) (b) AG with Ru, and (c) AG with Cu. AG results do not correlate strongly to Ru and CU results. Note, for Ru comparisons that include CD = 11.8 nm suggests its response in the UV is nonlinear with CD, while for Cu all six normalized sensitivities align, suggesting linearity in the UV.

In Fig. 6, the left column shows $S(\lambda)$ while the right column shows the corresponding $NS(\lambda)$. Rows correspond to the air gap, the Ru geometry, and the Cu geometry. A central message from these data for $t = 25$ nm is that the normalized sensitivity is relatively high for Cu in Fig 6(c) in a range between 175 nm $\leq \lambda \leq$ 300 nm, much higher than normalized sensitivity in the infrared. This roughly corresponds to the deep ultraviolet or DUV region. For Cu, the optical response is linear for the range 11.8 nm $\leq CD \leq$ 16.4 nm. Contrast this with the Ru data in Fig 6(b), where sensitivity is high if the comparison is against $CD = 11.8$ nm but for other CD pairings the normalized sensitivity is only reduced in the DUV. The normalized sensitivity data indicate that the optical response for Ru is nonlinear for 11.8 nm $\leq CD \leq$ 16.4 nm. Additionally, neither Ru nor Cu appear correlated with the air gap for all dimensions shown in Table 1.

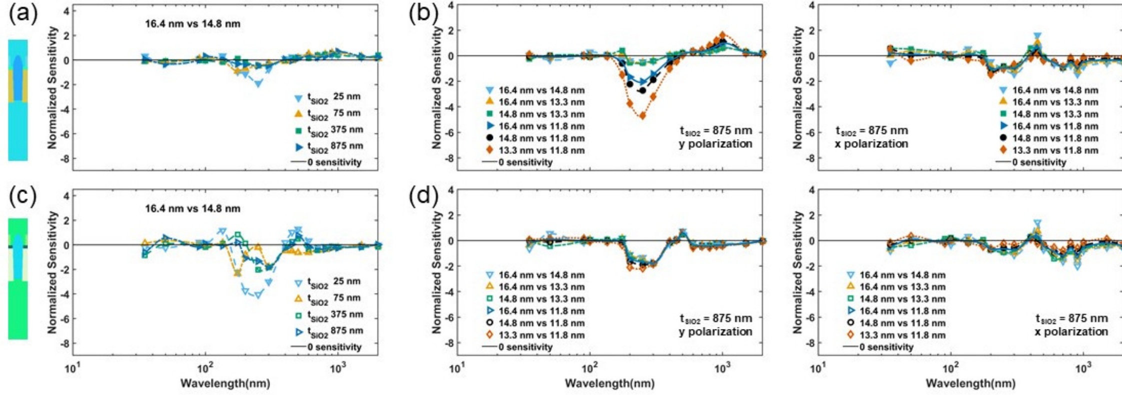

Figure 7. (left row) Normalized Sensitivities (NS) as a function of SiO_2 thickness and wavelength with X scan ($\theta_y = 0°$) and y polarization for $CD = 16.4$ nm vs $CD = 14.8$ nm. Rows correspond to (a) AG with Ru, and (c) AG with Cu. (b,d) NS at $t = 875$ nm for y polarization (center row) and x polarization (right row) and X scan. NS for Cu is optimized at the maximum SiO_2 thickness using ultraviolet y polarization; optimal polarization for Ru here is CD dependent.

While the deep ultraviolet wavelength range appears promising for Cu, recall that the SiO_2 thickness in Figs. 5 and 6 were purposely set to $t = 25$ nm to establish the most optimistic result as a baseline for comparison. In Fig. 7, the normalized sensitivities for Ru (top row) and Cu (bottom row) in the left column are presented as functions of increasing SiO_2 thickness for the CD pairing yielding the least favorable comparison for Ru at $t = 875$ nm as shown in Fig. 7(b). The prior optimisation of polarization and intensity angle for $t = 25$ nm (middle column) remains accurate for Cu but Ru is less straightforward. For comparisons against $CD = 11.8$ nm, the deep UV continues to be optimal over the infrared for Ru, put the other CDs tested require a polarization rotation for the UV wavelengths to yield $|NS|$ comparable to the infrared in either polarization. While the nonlinearity of the optical response from Ru yields complications, these are addressable in scatterfield microscopy by tailoring the polarization to ensure continued responsiveness to CD change in the DUV. Focus position can also be adjusted to better optimize these results.

4.3 Comparing MOL and BEOL Study Results

The central message of the MOL simulation study, the potential utility of deep ultraviolet wavelengths for current and future materials, differs from the BEOL study. Cu is common to both studies, and the maximum SiO_2 thickness in the MOL study $t = 875$ nm is comparable to the BEOL example's minimum buried layer thickness $t = 970$ nm, but the optical response in the deep ultraviolet differs. While an obvious difference between the studies is the presence of a periodic air gap in the MOL structure, it was shown that the air gap had minimal influence on the optical response once the metals were included. The key difference may then be the dense spacing of the Cu lines in the MOL compared to the isolated Cu lines in the BEOL. Specifically, with a pitch $p = 8250$ nm and Cu width of $CD = 1200$ nm, the edge-to-edge distance between Cu lines in these periodic RCWA simulations would exceed 10λ for $\lambda \leq$ 700 nm.

5. CONCLUSION

These two simulation studies suggest that our optics-based methods can contribute to the characterization of recently researched interconnect technologies for semiconductor metrology. Ultraviolet wavelengths between 175 nm to 300 nm may be well positioned to measure the nanoscale line widths of MOL buried Cu and possibly Ru lines at the dimensions and pitch required for semiconductor fabrication in the next decade, due in part to their optical density. For example, our $\lambda = 193$ nm high-magnification optical platform may be applicable but additional simulation would be required at the specific numerical aperture range (NA = 0.13 to 0.74) of its catadioptric objective lens. Simulations indicate that optically isolated, large buried features at the back-end-of-line would not be readily observable using the ultraviolet and must be investigated using longer wavelengths. These straightforward studies identify which wavelengths and instruments may be ill-suited for this research area (*e.g.*, our $\lambda = 450$ nm microscope) while prioritizing which wavelengths should be pursued in greater detail in more computationally expensive, three-dimensional electromagnetic simulations that also include preceding interconnect layers.

ACKNOWLEDGMENTS

The author thanks NIST colleagues Joeseph J. Kopanski and Yaw Obeng for discussion on the BEOL. I also thank Martin Y. Sohn and Thomas A. Germer for discussions and for development of and access to, respectively, the NIST λ=193 nm Microscope and to an implementation of RCWA code. I thank former colleague Francois Goasmat for code parallelization.

REFERENCES

[1] Orji, N. G., Badaroglu, M., Barnes, B. M., Beitia, C., Bunday, B. D., Celano, U., Kline, R. J., Neisser, M., Obeng, Y., and Vladar, A., "Metrology for the next generation of semiconductor devices," *Nature Electronics* **1**(10), 532–547 (2018).

[2] Sunday, C. E., Veksler, D., Cheung, K. C., and Obeng, Y. S., "Microwave evaluation of electromigration susceptibility in advanced interconnects," *Journal of Applied Physics* **122**(17), 174504 (2017).

[3] You, L., Ahn, J.-J., Obeng, Y. S., and Kopanski, J. J., "Subsurface imaging of metal lines embedded in a dielectric with a scanning microwave microscope," *Journal of Physics D: Applied Physics* **49**(4), 045502 (2015).

[4] Sohn, M. Y., Barnes, B. M., and Silver, R. M., "Design of angle-resolved illumination optics using nonimaging bi-telecentricity for 193 nm scatterfield microscopy," *Optik* **156**, 635–645 (2018).

[5] Leśniewska, A., Pedreira, O. V., Lofrano, M., Murdoch, G., van der Veen, M., Dangol, A., Horiguchi, N., Tőkei, Z., and Croes, K., "Reliability of a DME Ru semidamascene scheme with 16 nm wide airgaps," in [*2021 IEEE International Reliability Physics Symposium (IRPS)*], 1–6, IEEE (2021).

[6] Germer, T. A., "Effect of line and trench profile variation on specular and diffuse reflectance from a periodic structure," *J. Opt. Soc. Am. A* **24**, 696–701 (Mar 2007).

[7] Moharam, M. G., Pommet, D. A., Grann, E. B., and Gaylord, T. K., "Stable implementation of the rigorous coupled-wave analysis for surface-relief gratings: enhanced transmittance matrix approach," *J. Opt. Soc. Am. A* **12**, 1077–1086 (May 1995).

[8] Lalanne, P. and Morris, G. M., "Highly improved convergence of the coupled-wave method for TM polarization," *J. Opt. Soc. Am. A* **13**, 779–784 (Apr 1996).

[9] Barnes, B. M., Attota, R., Quintanilha, R., Sohn, Y., and Silver, R. M., "Characterizing a scatterfield optical platform for semiconductor metrology," *Measurement Science and Technology* **22**(2), 024003 (2010).

[10] Silver, R. M., Barnes, B. M., Attota, R., Jun, J., Stocker, M., Marx, E., and Patrick, H. J., "Scatterfield microscopy for extending the limits of image-based optical metrology," *Appl. Opt.* **46**, 4248–4257 (Jul 2007).

[11] Barnes, B. M., Henn, M.-A., Sohn, M. Y., Zhou, H., and Silver, R. M., "Appraising the extensibility of optics-based metrology for emerging materials," *ECS Transactions* **92**, 73–84 (Jul 2019).

[12] Zhang, N. F., Barnes, B. M., Zhou, H., Henn, M.-A., and Silver, R. M., "Combining model-based measurement results of critical dimensions from multiple tools," *Measurement Science and Technology* **28**, 065002 (Apr 2017).

[13] Lynch, D. W. and Hunter, W., "Comments on the optical constants of metals and an introduction to the data for several metals," in [*Handbook of Optical Constants of Solids*], Palik, E. D., ed., 275–367, Academic Press, Burlington (1997).

[14] Rodríguez-de Marcos, L. V., Larruquert, J. I., Méndez, J. A., and Aznárez, J. A., "Self-consistent optical constants of SiO_2 and Ta_2O_5 films," *Opt. Mater. Express* **6**, 3622–3637 (Nov 2016).

[15] Lynch, D. W. and Hunter, W., "An introduction to the data for several metals," in [*Handbook of Optical Constants of Solids*], Palik, E. D., ed., 341, Academic Press, Boston (1998).

[16] Edwards, D. F., "Silicon (Si)*," in [*Handbook of Optical Constants of Solids*], Palik, E. D., ed., 547–569, Academic Press, Burlington (1997).

[17] Philipp, H. R., "Optical properties of silicon nitride," *Journal of The Electrochemical Society* **120**(2), 295 (1973).

[18] Pflüger, J., Fink, J., Weber, W., Bohnen, K. P., and Crecelius, G., "Dielectric properties of TiC_x, TiN_x, VC_x, and VN_x from 1.5 to 40 eV determined by electron-energy-loss spectroscopy," *Phys. Rev. B* **30**, 1155–1163 (Aug 1984).